Journal of Non-Newtonian Fluid Mechanics, 40 (1991) 231–260
Elsevier Science Publishers B.V., Amsterdam

Newtonian and non-Newtonian flow in a channel obstructed by an antisymmetric array of cylinders

G. Georgiou [a], S. Momani [b], M.J. Crochet [a] and K. Walters [b]

[a] *Unité de Mécanique Appliquée, Université Catholique de Louvain, 1348 Louvain-la-Neuve (Belgium)*

[b] *Department of Mathematics, University College of Wales, Aberystwyth SY23 3BZ (U.K.)*

(Received December 14, 1990; in revised form March 11, 1991)

Abstract

Consideration is given to the flow of Newtonian and non-Newtonian elastic liquids in a channel obstructed by an antisymmetric array of cylinders. Experiments are carried out on Newtonian maltose-syrup/water mixtures and a variety of non-Newtonian liquids, including constant-viscosity Boger fluids and shear-thinning aqueous polymer solutions. In one case, the polymer is polyacrylamide and the shear thinning is accompanied by high normal stresses and high extensional-viscosity levels. In another case, the polymer is the more rigid xanthan gum and the normal-stress and extensional-viscosity levels are accordingly much lower. The details of the flow are investigated by means of a laser technique, which permits an overall picture to be obtained with relative ease. The resistance to flow caused by the positioning of the cylindrical obstructions is also investigated through the pressure gradient/flow rate data. It is concluded that the tortuous geometry and rheology combine to produce significant viscoelastic effects with regard to both the general flow field and 'resistance to flow'.

A finite element technique is employed to simulate numerically the observed flows. Significant success is claimed in qualitatively reproducing the viscoelastic behaviour in the model geometry. The quantitative agreement between experiment and theory is considered to be satisfactory, within the acknowledged limitations of present-day viscoelastic simulations.

Keywords: antisymmetric array of cylinders; Boger fluids; finite element technique

1. Introduction

The work contained in this paper may be viewed as a part of an ongoing attempt to understand the way highly-elastic liquids behave in complex geometries (see, for example, Refs. 1–5). In previous studies, dramatic changes in flow characteristics have been observed, brought about by a combination of shear thinning and strong viscoelastic effects. Attempts to simulate these changes have been marginally successful, although any *quantitative* agreement between experiment and theory has been elusive. The present paper indicates that significant progress is being made, most notably in the power of the numerical codes that are now available. The final chapter in the long search for agreement between theory and experiments has certainly not been written, but at least some success can be claimed.

The particular flow under investigation in the present paper is the tortuous one brought about by the antisymmetric positioning of an array of equally spaced cylinders in a channel (see Fig. 1). The geometry is characterized by a series of narrow and wide channels caused by the positioning of the cylindrical barriers, thus simulating in a simple way the tortuous geometries encountered in a variety of applications of significant practical importance, including flow through porous media as encountered in Enhanced Oil Recovery (EOR) (cf. Ref. 5).

The present work may be viewed as a continuation of the study of Jones and Walters [5] who were mainly concerned with the extensional-viscosity levels found in polymeric displacement fluids of use in EOR and their importance in determining flow characteristics. Alternatively, the present paper may be seen as the continuation of the work of Binding et al. [3] where a quantitative agreement between experiment and numerical simula-

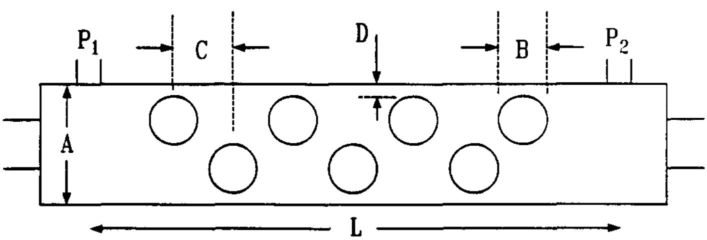

Dimensions of model geometries: (mm)

Geometry	A	B	C	D	L
W1	23	12.5	33.75	2.5	326
W2	23	12.5	33.75	3.5	326

Fig. 1. Schematic diagram of the geometries, with the relevant dimensions.

tion was sought for a number of complex flows involving abrupt changes in geometry. The flow domain discussed in the present work is certainly complex with a strong 'Lagrangian unsteadiness' but it is nevertheless free of the abrupt changes in geometry (like re-entrant corners) which figured so prominently in the earlier work.

Published experimental work [5;6, p. 96] on the flow geometry shown in Fig. 1 indicates that extensional-viscosity effects become very important beyond a critical set of conditions, after which the fluid is often reluctant to pass through the narrow channels, on account of the high resistance to flow in the contraction regions between the cylinders and the walls. Such behaviour is further explored in the present paper, both experimentally and theoretically.

2. Experiment

2.1. Apparatus

Figure 2 is a schematic diagram of the apparatus. The fluid from the reservoir is circulated by means of a peristaltic pump. The fluctuations in the flow caused by the peristaltic nature of the pump are smoothed by means of a damping bottle. The flow after the smoothing bottle is essentially steady and the liquid passes into the test geometry and thence back to the reservoir to be recirculated. Flow rates are determined by a conventional catch-and-measure technique and the pressure gradient across the geometry

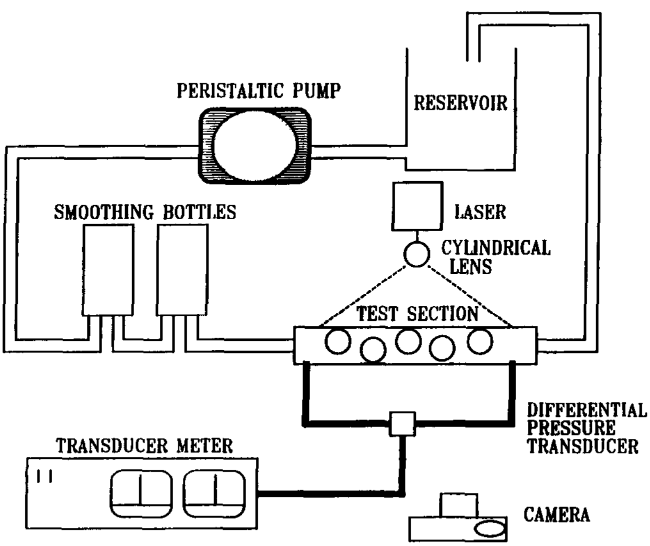

Fig. 2. Schematic diagram of the experimental set-up.

is measured by a differential pressure transducer acting at suitable points upstream and downstream of the obstruction or by two flush-mounted pressure transducers acting on either side of the obstacles (cf. Ref. 5).

The basic geometry is that shown in Fig. 1, with two values of D available (2.5 and 3.5 mm). The narrow gap geometry is denoted by $W1$ and the wider gap geometry by $W2$. The third dimension in each case is 25 mm and the flow is considered to be basically two-dimensional. The validity of this assumption has been checked in the course of the present experiments (see Section 2.3).

In previous papers [1–5], we have resorted to a simple flow-visualization technique which uses an expanded laser beam as an illuminating source. Small tracer particles, contained in and moving with the flow, give a visual representation of the flow as they are illuminated by the laser light and photographed. In the present study, polyvinyl chloride particles with a density of 1.4 g cm^{-3} are used in the experiments on Newtonian and Boger fluids and a high-density polyethylene powder with a density of 0.94 g cm^{-3} is used in the experiments on the aqueous polymer solutions. The grain size of the powders when in suspension is of the order of 0.1 mm in diameter, and except in extreme circumstances (cf. Ref. 3) it is reasonable to assume that the particles faithfully follow the streamlines. All the experiments were carried out at 20 °C.

2.2. Test fluids

Fluids with four basic types of behaviour have been used in the current experiments (cf. Refs. 1–5):

(i) Constant-viscosity Newtonian liquids. These were mixtures of water and maltose syrup (supplied by CPC, U.K.). The letter N is used to denote Newtonian liquids.

(ii) 'Weakly elastic' shear-thinning liquids. These were 3% aqueous solutions of xanthan gum (Keltrol F, supplied by Kelco International Ltd) (see Ref. 7 for a detailed study of the rheology of this solution). The letter X is used to denote the xanthan-gum solution.

(iii) 'Highly elastic' shear-thinning liquids. These were 2% aqueous solutions of polyacrylamide (E10 grade supplied by Allied Colloids Ltd, U.K.) (see Ref. 7 for a detailed study of the rheology of this solution). The letter P is used to denote the polyacrylamide solution.

(iv) Highly elastic constant-viscosity (Boger) fluids (cf. Ref. 8). These were fairly dilute (~ 0.1%) solutions of polyacrylamide in a highly viscous solvent (a mixture of water and maltose syrup). Boger fluids are denoted by the letter B.

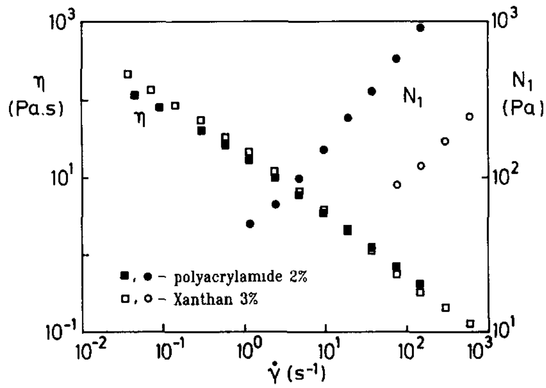

Fig. 3. Steady shear data for the 2% polyacrylamide solution and the 3% xanthan-gum solution (see also 7).

In a steady simple shear flow with Cartesian velocity components given by

$$v_x = \dot{\gamma} y, \; v_y = v_z = 0, \tag{1}$$

where $\dot{\gamma}$ is a constant shear rate, the corresponding stress distribution can be written in the form [6]

$$\left.\begin{aligned} \sigma_{xy} &= \sigma = \dot{\gamma}\eta(\dot{\gamma}), \\ \sigma_{xx} - \sigma_{yy} &= N_1(\dot{\gamma}), \\ \sigma_{yy} - \sigma_{zz} &= N_2(\dot{\gamma}), \end{aligned}\right\} \tag{2}$$

where σ is the shear stress, η the shear viscosity and N_1 and N_2 are the first and second normal stress differences, respectively. In conventional rheometry it is customary to concentrate attention on σ (or η) and N_1. Representa-

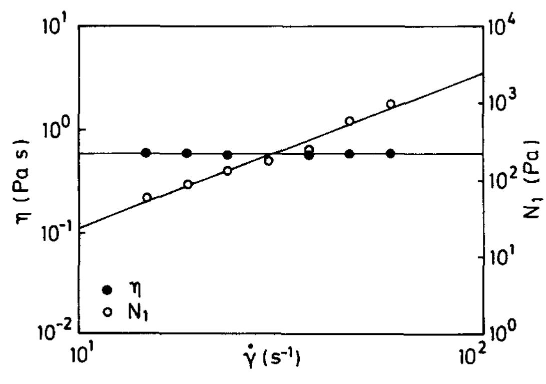

Fig. 4. Steady shear data for Boger fluid B112 (20 °C).

TABLE 1

Estimated constants for the Newtonian and Boger fluids

Fluid	ρ (g cm^{-3})	η (Pa s)	λ (s)
N11	1.31	1.28	–
N12	1.23	0.04	–
B112	1.3	0.6	0.22

tive graphs of η and N_1 for some of the liquids used in the present experiments are contained in Figs. 3 and 4 (cf. Refs. 5–7). The viscosity η is constant for the Newtonian fluids and is (approximately) constant for the Boger fluids. For the 3% xanthan-gum solution and the 2% polyacrylamide

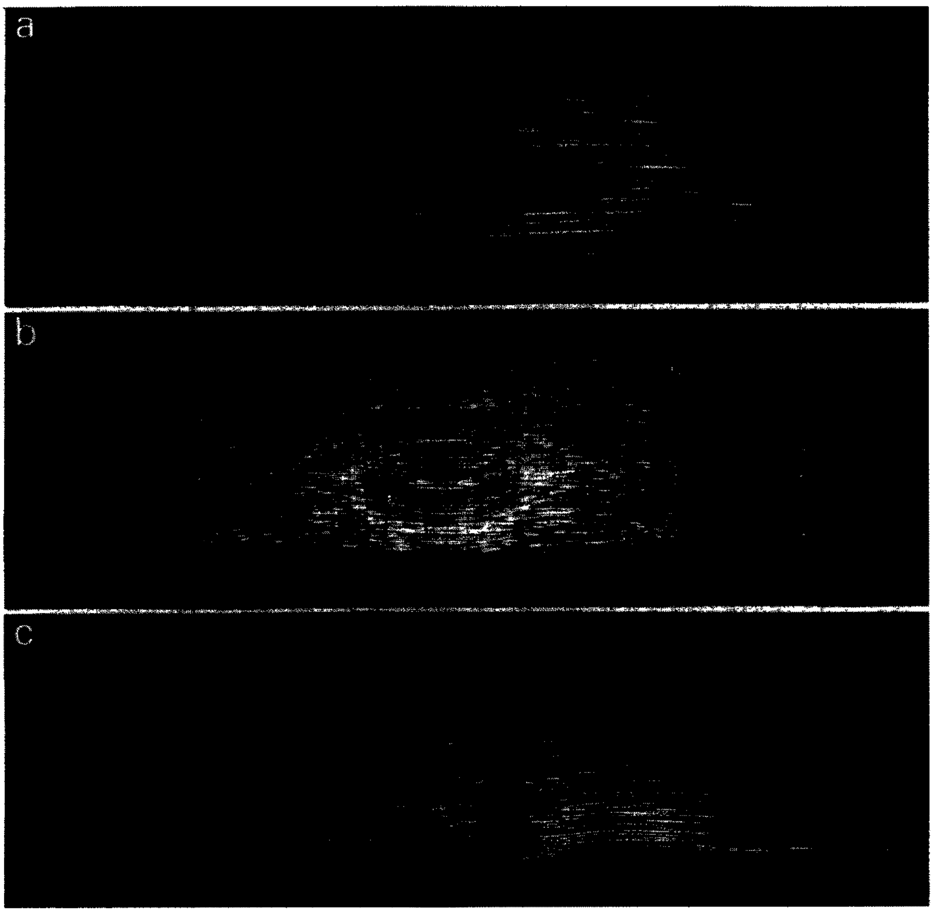

Fig. 5. Flow visualization of the three-dimensional effect for Newtonian liquid N11 in geometry $W1$. (a) Front; (b) middle; (c) back.

solution, η decreases rapidly with shear rate. The two concentrations were in fact chosen such that the shear viscosities are very similar over a wide shear-rate range [7].

The normal stress difference N_1 is zero for the Newtonian fluids. For the B and P fluids N_1 is non-zero and can be higher than the shear stress σ, indicating substantial viscoelastic behaviour. For Boger fluids, N_1 is a quadratic function of $\dot{\gamma}$ over a reasonable shear-rate range and it is customary to define a characteristic relaxation time λ for these fluids through (cf. Refs. 1–3)

$$N_1 = 2\eta\lambda\dot{\gamma}^2. \tag{3}$$

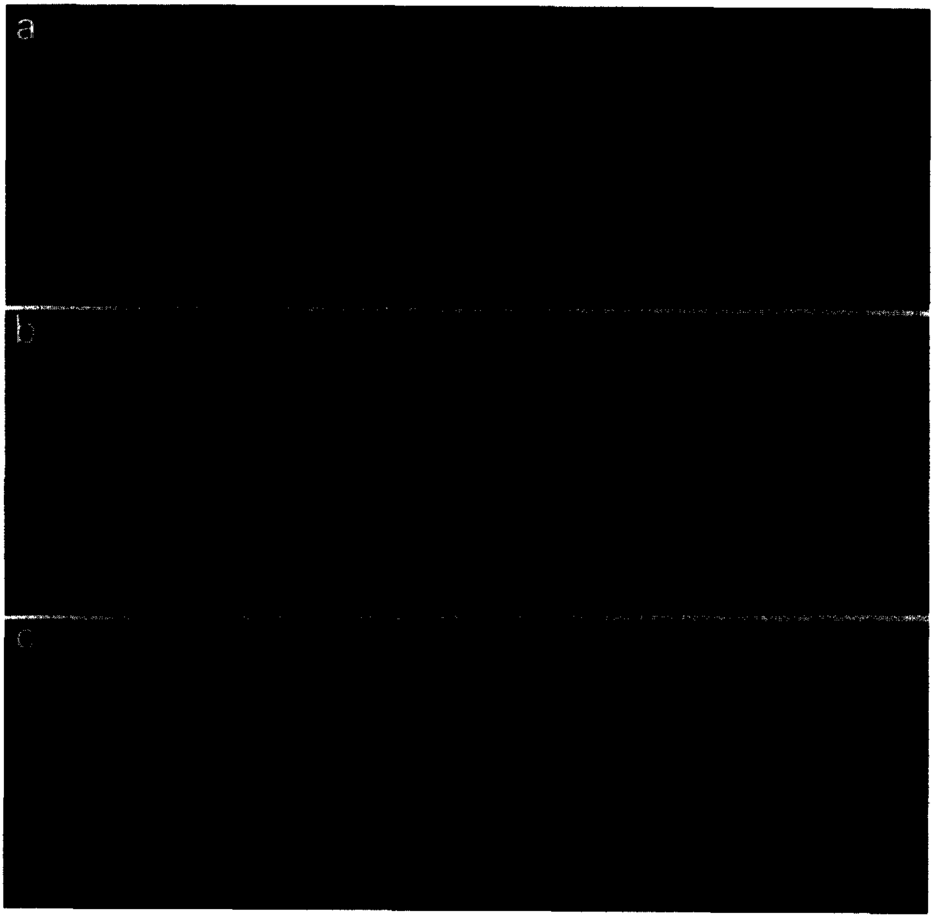

Fig. 6. Flow visualization of the three-dimensional effect for 2% polyacrylamide solution in geometry $W1$. (a) Front; (b) middle; (c) back.

Two dimensionless numbers may now be defined. First, the Reynolds number Re given by

$$Re = \rho \frac{UA}{2\bar{\eta}}, \tag{4}$$

where ρ is the density, U is the mean velocity in the channel, A is the width of the channel and $\bar{\eta}$ is the viscosity at the mean shear rate $\dot{\gamma}_m$, given by

$$\dot{\gamma}_m = \frac{2U}{A}. \tag{5}$$

Secondly, the Weissenberg number We is defined by

$$We = 2\frac{\lambda U}{A}. \tag{6}$$

Table 1 contains estimates of the constants for the Newtonian and Boger fluids used in the present experiments.

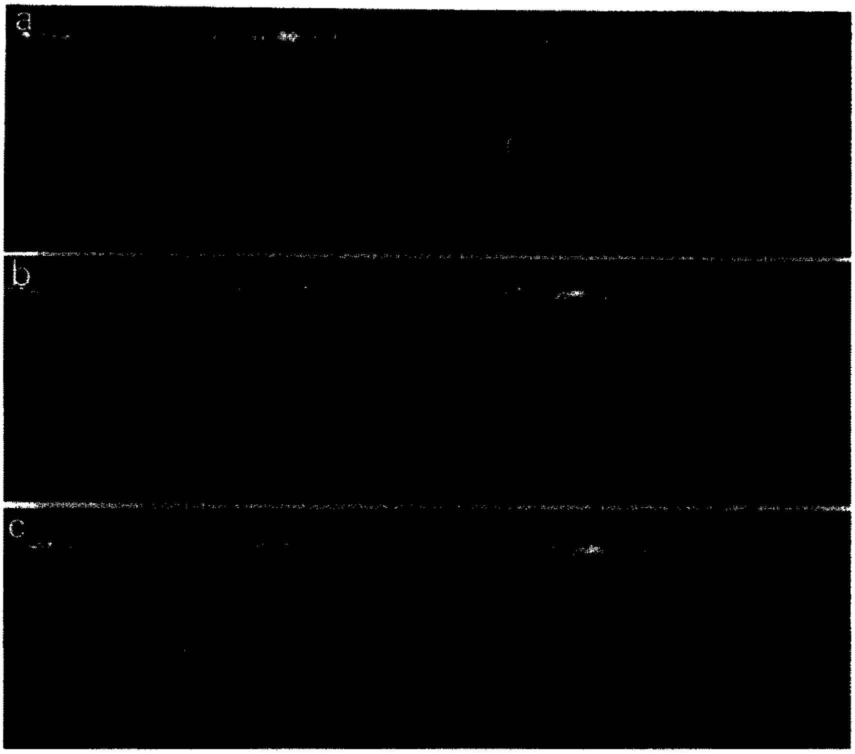

Fig. 7(i) Flow visualization of the three-dimensional effect for N12 in the central plane of geometry $W1$. (a) $Re = 31.0$; (b) $Re = 41.3$; (c) $Re = 55.1$.

In a uniaxial extensional flow given by

$$v_x = \dot{\epsilon} x, \; v_y = -\frac{\dot{\epsilon} y}{2}, \; v_z = -\frac{\dot{\epsilon} z}{2}, \tag{7}$$

where $\dot{\epsilon}$ is a constant extensional strain rate, the corresponding stress distribution can be written

$$\left.\begin{aligned} &\sigma_{ik} = 0 \text{ for } i \neq k, \\ &\sigma_{xx} - \sigma_{yy} = \sigma_{xx} - \sigma_{zz} = \dot{\epsilon}\eta_E(\dot{\epsilon}), \end{aligned}\right\} \tag{8}$$

where η_E is the uniaxial extensional viscosity.

For Newtonian liquids, η_E is three times the shear viscosity η. For some polymer solutions, like the polyacrylamide solutions used in the present experiments, η_E can be a strong increasing function of $\dot{\epsilon}$. It is generally conceded that in many complex situations, the extensional behaviour of the fluid can strongly affect the flow characteristics.

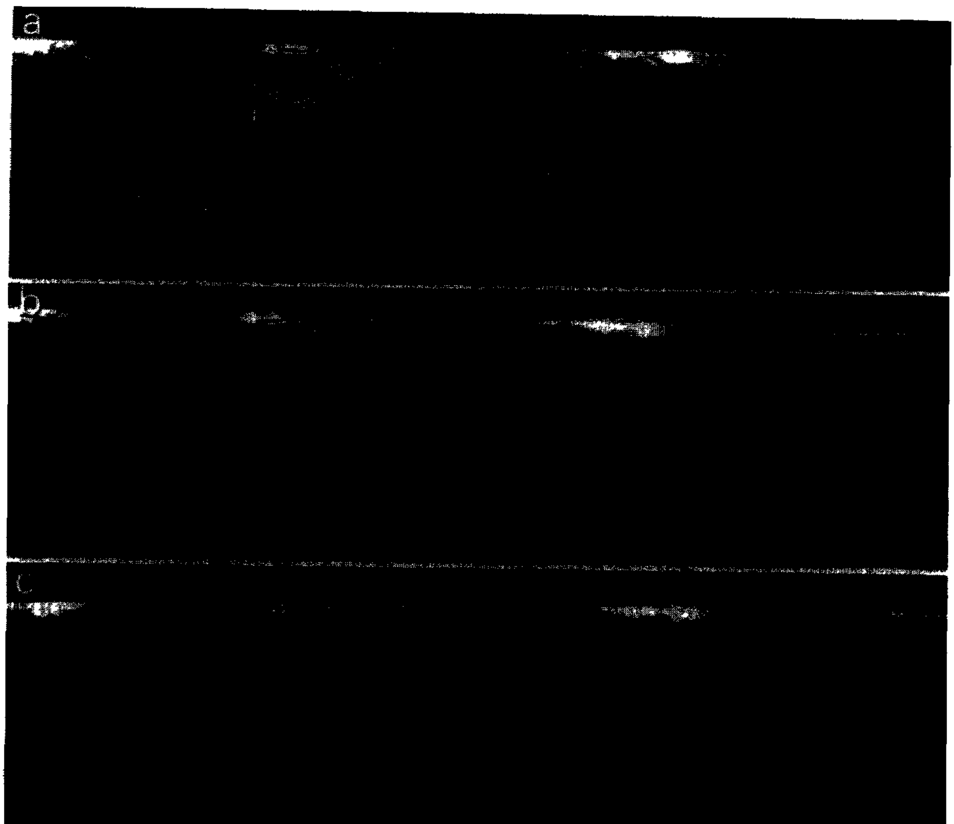

Fig. 7 (ii) Flow visualization for liquid N12 near the boundary wall of geometry *W*1, (a) *Re* = 31.0; (b) *Re* = 41.3; (c) *Re* = 55.1.

The determination of η_E in the case of polymer solutions is very difficult and the value of the various available experimental methods is under careful scrutiny at the present time (cf. Ref. 9). What is incontrovertible, however, is that some dilute polymer solutions like the B and P series offer significant resistance to stretching deformations, while others, like the X and N series, do not. The general consequences of this observation for the type of flows considered in the present work have been adequately dealt with by Jones and Walters [5].

We note that since the 2% polyacrylamide solution and the 3% xanthan-gum solution have similar shear viscosities, a comparison of their behaviour in complex flows is useful in estimating the effect of fluid elasticity on flow characteristics in the case of shear-thinning fluids.

Finally, the behaviour of the more dilute xanthan-gum solutions considered by Jones and Walters [5] is discussed in the section on numerical simulation.

2.3. *Experimental results*

In the interpretation of the experimental results, it is assumed that the flow is two-dimensional. There is, therefore, a need to investigate whether this is a meaningful assumption. Accordingly, two types of experiment were carried out to investigate any three-dimensional components in the flow. First, the laser beam was turned through 90° and the flow structure investigated in the narrow gap between the top wall and the cylinders and also near the centre of the channel, where some of the domain is clearly taken up by the cylinders themselves. Figures 5 and 6 show that, for both a Newtonian and an elastic polymer solution in geometry $W1$, the streamlines are not straight and parallel as would be required for a truly two-dimensional flow. The three-dimensional effect is even more pronounced in the photographs shown in Fig. 7 for a Newtonian liquid with the usual laser positioning. Here the laser beam illuminates the central plane in Fig. 7(i) (as in the vast majority of the cases considered) while in Fig. 7(ii) the laser beam illuminates a plane near the bonding wall. The interesting appearance of an *upstream* vortex is clearly visible in Fig. 7(ii); but this is much less pronounced in Fig. 7(i). This is clear evidence of a three-dimensional component in the flow. We remark that the three-dimensional effect increased with the Reynolds number.

Clearly the presence of these three-dimensional effects makes *quantitative* agreement between theory and experiment difficult, but the flow structure viewed in the central plane should still give a reasonable picture of the flow to be expected in a truly two-dimensional flow.

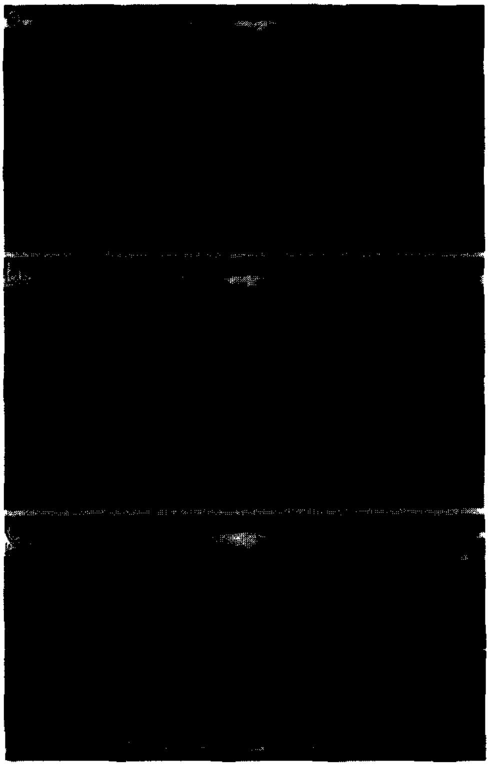

Fig. 8. Flow visualization for liquid N12 in geometry $W2$. (a) $Re = 21.7$; (b) $Re = 28$; (c) $Re = 44.8$.

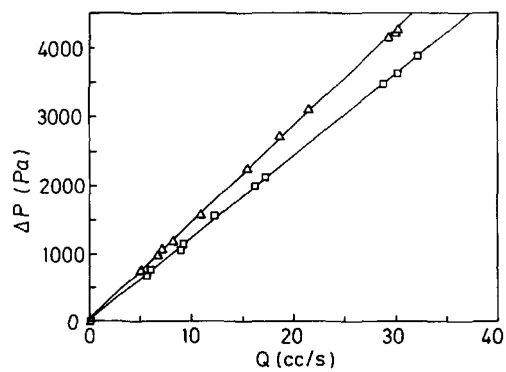

Fig. 9. Pressure drop ΔP vs. flow rate Q data for Newtonian liquid N11 in geometries $W1$ (□) and $W2$ (Δ).

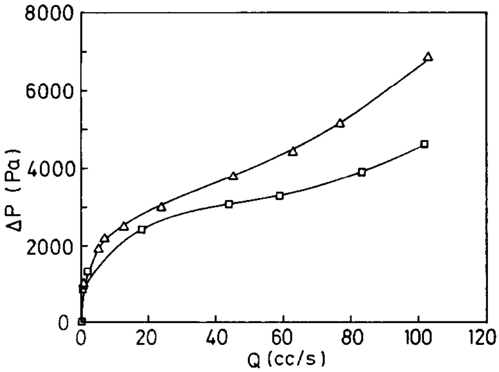

Fig. 10. Pressure drop vs. flow rate data for a 2% polyacrylamide solution in geometries *W*1 (□) and *W*2 (Δ).

Photographs of the streamlines for a Newtonian liquid in geometry *W*2 are included in Fig. 8 for increasing Reynolds number. The appearance of downstream vortices at the higher Reynolds numbers is clearly evident.

Figure 9 contains (ΔP, Q) data for Newtonian liquids in geometries *W*1 and *W*2, ΔP being the pressure drop across the geometry (see Fig. 1). It is clear that it is easier to pump Newtonian liquids through the geometry with the narrowest gap D between the cylinders and the wall (i.e. geometry *W*1). Figure 10 for a 2% aqueous polyacrylamide solution shows the same general trend for varying gap D.

Figures 11 and 12 include a comparison of the pressure drop/flow rate behaviour of the aqueous solutions of polyacrylamide and xanthan gum. At low flow rates, the resistance to flow is similar for both liquids. At intermediate flow rates, the more elastic polyacrylamide solution shows a mea-

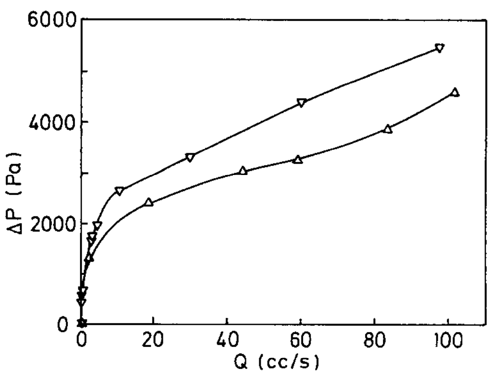

Fig. 11. Pressure drop vs. flow rate data for a 2% aqueous polyacrylamide solution (Δ) and a 3% aqueous xanthan-gum solution (∇) in geometry *W*1.

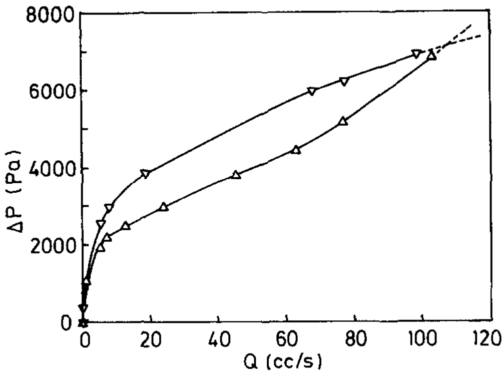

Fig. 12. Pressure drop vs. flow rate data for a 2% aqueous polyacrylamide solution (Δ) and a 3% aqueous xanthan-gum solution (∇) in geometry *W*2.

sure of drag reduction, before the extensional-viscosity effect for this solution results in an upturn in the appropriate curve, with the consequent possibility of a cross-over in the curves for the two solutions. Such a cross-over is already in evidence for geometry *W*2, but the available experimental range for geometry *W*1 was not sufficient to reach the cross-over point in this case.

In the case of the Boger fluids, it is convenient to plot the 'resistance' $\Delta P/Q$ against Q. In Figs. 13 and 14 we see that the resistance initially decreases with Q (compared to that expected for a *Newtonian* liquid of the same viscosity) and then increases significantly. This is a striking example of the validity of the Walters–Barnes [10] conjecture that viscoelasticity is associated with an initial decrease in drag for low flow rates followed by a significant increase at higher flow rates. The increase is generally associated with the high extensional viscosities of the elastic liquids.

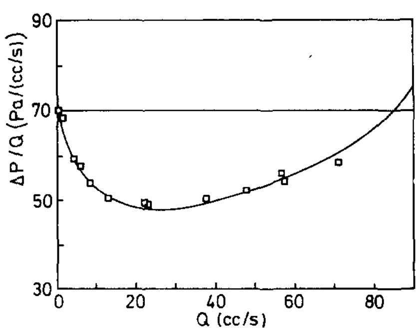

Fig. 13. $\Delta P/Q$ against Q data for Boger fluid B112 in geometry *W*1.

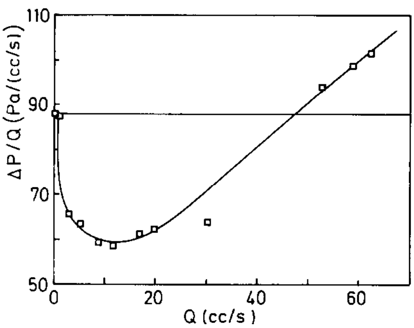

Fig. 14. $\Delta P/Q$ against Q data for Boger fluid B112 in geometry $W2$.

Interestingly, over the examined range of Reynolds numbers of the experiments, the flow field for the B liquids is not *significantly* affected by either viscoelasticity or Reynolds number (see Figs. 15 and 16).

From previous work with *very* dilute polymer solutions [5] it is known that the extensional-viscosity effect is so dominant that often virtually no

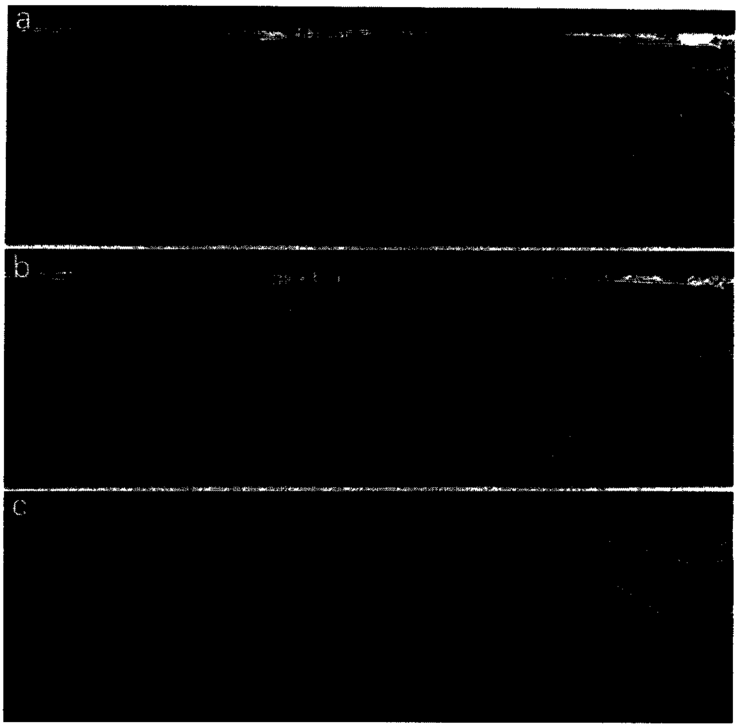

Fig. 15. Flow visualization for Boger fluid B112 in geometry $W1$. (a) $Re = 0.65$; (b) $Re = 1.46$; (c) $Re = 3.05$.

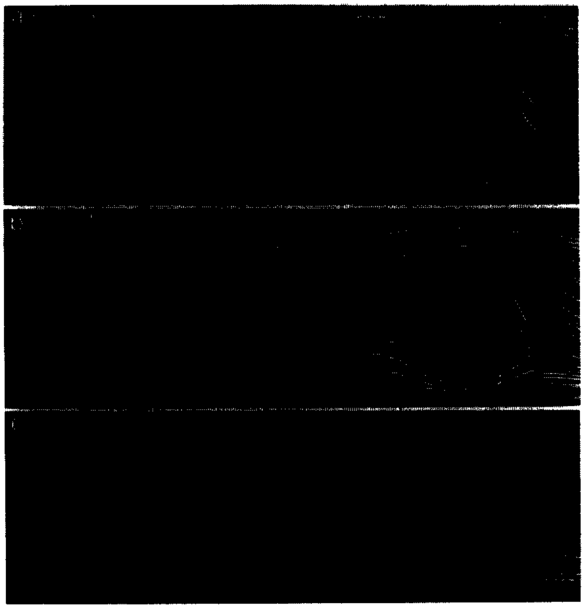

Fig. 16. Flow visualization for Boger fluid B112 in geometry $W2$. (a) $Re = 0.51$; (b) $Re = 1.3$; (c) $Re = 2.77$.

fluid can enter the narrow channels between the cylinders and the walls. With the more concentrated 2% solutions studied here, the general phenomenon is still evident (see Figs. 17 and 18), but the scale of the effect over the available flow rate range is not as dramatic as in the very dilute P liquids discussed in Ref. 5.

3. Numerical simulation

3.1. General equations

To avoid solving the flow problem over the entire physical domain of Fig. 1, periodicity is assumed near the middle of the channel where the photographs are taken. Therefore, we consider the flow in the geometry shown in Fig. 19. For steady incompressible flow in the absence of body forces, the governing field equations are

$$\rho \boldsymbol{v} \cdot \nabla \boldsymbol{v} = -\nabla p + \nabla \cdot \boldsymbol{T} \tag{9}$$

$$\nabla \cdot \boldsymbol{v} = 0, \tag{10}$$

where $\boldsymbol{v}$ is the velocity vector, p an arbitrary isotropic pressure and $\boldsymbol{T}$ is the extra stress tensor defined by

$$\sigma = -p\boldsymbol{I} + \boldsymbol{T}. \tag{11}$$

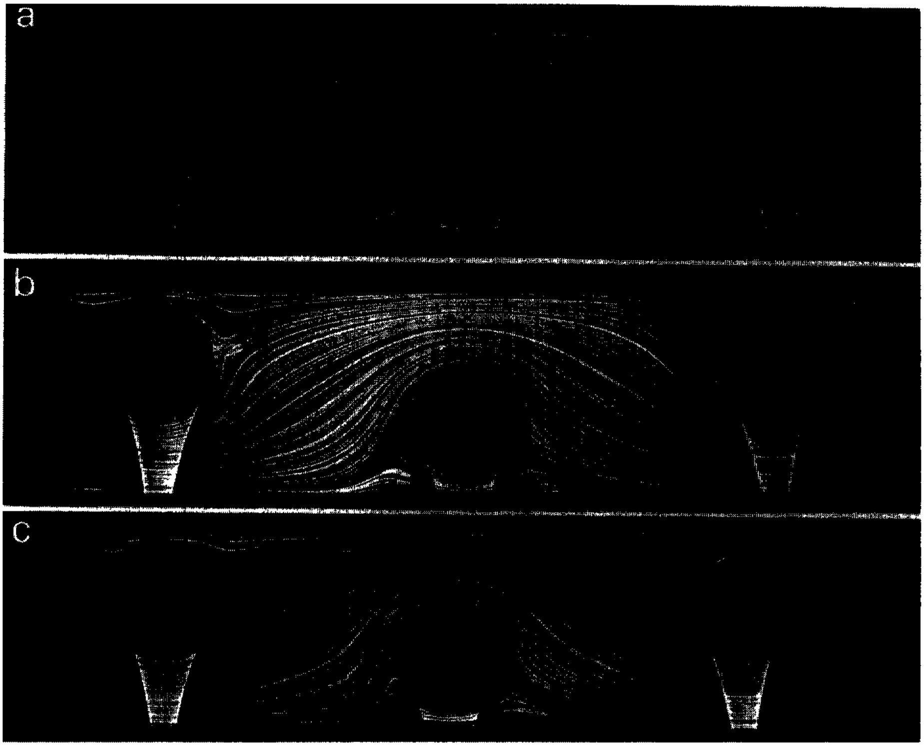

Fig. 17. Flow visualization for a 2% polyacrylamide solution in geometry $W1$. (a) $Q = 23.3$; (b) 27.8; (c) 44 ($cm^3\ s^{-1}$).

In addition to the field eqns. (9) and (10), we require constitutive equations to describe the response of the various elastic liquids discussed in Section 2. For the Newtonian fluids we have simply

$$\boldsymbol{T} = 2\eta \boldsymbol{d}, \tag{12}$$

where the rate-of-strain tensor $\boldsymbol{d}$ is defined by

$$\boldsymbol{d} = \tfrac{1}{2}\left[(\nabla \boldsymbol{v}) + (\nabla \boldsymbol{v})^T\right], \tag{13}$$

where T denotes the transpose.

For the shear-thinning and weakly-elastic xanthan-gum solutions, we employ the Bird–Carreau model with the viscosity η in eqn. (12) (now considered to be a function of I_2, the second invariant of $\boldsymbol{d}$) given by

$$\eta = \eta_\infty + (\eta_0 - \eta_\infty)\left[1 + K^2 I_2\right]^{(n-1)/2}; \tag{14}$$

where η_0, η_∞, K and n are material parameters. For the 1500 ppm X fluid used by Jones and Walters [5] we take

$$\eta_0 = 10 \text{ Pa s},\ \eta_\infty = 0,\ K = 1425 \text{ s},\ n = 0.5.$$

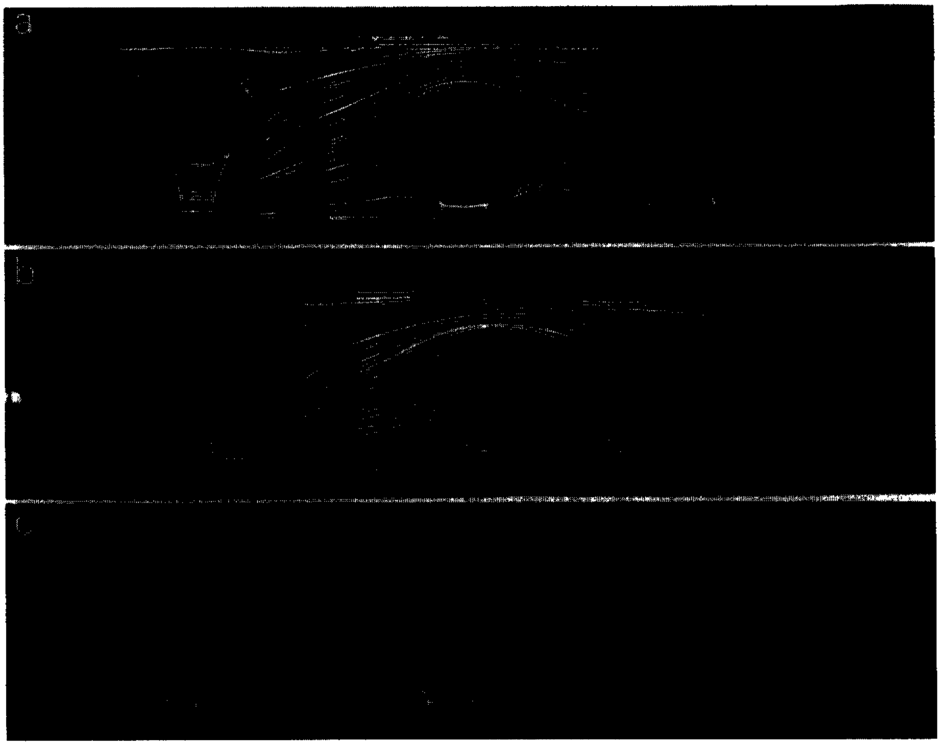

Fig. 18. Flow visualization for a 2% polyacrylamide solution in geometry $W2$. (a) $Q = 25.2$; (b) 33.4; (c) 56.2 ($cm^3\ s^{-1}$).

To simulate viscoelastic flow in the model geometry we employ the Oldroyd-B model, customarily used for the constant-viscosity Boger fluids. (The flow simulation of the elastic and shear-thinning P fluids is not in the

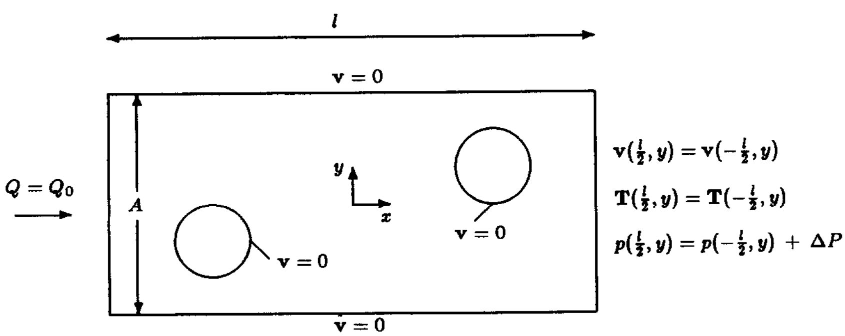

Fig. 19. Geometry and boundary conditions for the periodic flow.

focus of the present work.) The extra-stress tensor is decomposed as follows (cf. [11]):

$$\boldsymbol{T} = \boldsymbol{T}_1 + \boldsymbol{T}_2, \tag{15}$$

$$\boldsymbol{T}_1 + \lambda \overset{\nabla}{\boldsymbol{T}}_1 = 2\eta_1 \boldsymbol{d}, \tag{16}$$

$$\boldsymbol{T}_2 = 2\eta_2 \boldsymbol{d}, \tag{17}$$

where η_1, η_2 and λ are constants and the symbol ∇ denotes the upper convected derivative [12]. The shear viscosity is given by $\eta = \eta_1 + \eta_2$ and the first normal stress difference N_1 by eqn. (3) with λ replaced by $\lambda\eta_1/(\eta_1 + \eta_2)$. For the uniaxial extensional viscosity we have

$$\eta_E = 3\eta_2 + \frac{2\eta_1}{(1 - 2\dot{\epsilon}\lambda)} + \frac{\eta_1}{(1 + \dot{\epsilon}\lambda)}. \tag{18}$$

The ratio $\eta_2/(\eta_1 + \eta_2)$ is the ratio of the retardation time to the relaxation time; a value of $1/8$ is taken for this ratio.

The boundary conditions are also shown in Fig. 19. A no-slip condition is assumed on all solid surfaces while periodicity relates the unknowns at the inlet and outlet. Respective nodal velocity and extra-stress components (only for the elastic fluids) are equal and nodal pressures are required to differ by the unknown pressure drop ΔP. Imposing the flow rate Q provides the additional constraint required to determine ΔP.

To non-dimensionalize the governing equations, we scale the velocity components by the average velocity in the channel U, the lengths by the channel half-width $A/2$ and the pressure and the stress components by $2\bar{\eta}U/A$. This scaling yields the two dimensionless numbers, *Re* and *We*, defined in eqns. (4) and (6).

3.2. Numerical method

The finite element method is used for all the numerical solutions of this work. For the generalized-Newtonian flows, the pressure and the velocity components are interpolated by means of bilinear and biquadratic shape functions, respectively. When viscoelastic models are used, one has also to expand the extra-stress components in terms of appropriate shape functions. We use the mixed finite element developed by Marchal and Crochet [13] which is highly stable in solving various viscoelastic problems at high values of the Weissenberg number [13,14]. This element is based on a 4×4 sub-linear interpolation for the extra-stress components and satisfies the Babuska–Brezzi conditions for stability [15,16].

Another important feature of the method is the use of streamline upwinding [17]. This technique stabilizes the numerical results by means of artificial stress diffusivity along the streamlines. As pointed out in Ref. 18, the artificial stress diffusivity vanishes as the element size goes to zero and the method converges linearly with mesh refinement. More details about the use of streamline upwinding for viscoelastic flows can be found in Refs. 13, 18 and 19.

Imposing the flow rate at the inlet provides the additional equation needed to calculate the unknown pressure drop. Details about the modifications required to handle periodic flows with the finite element method are given by Delvaux [19]. The periodicity assumption eliminates the need for solving the problem over the entire physical domain. It should be added, however, that the frontal width doubles when periodic boundary conditions are applied and a row-by-row element numbering is performed [19].

3.3. *Numerical results*

The three meshes constructed for the numerical calculations are shown in Fig. 20 and their main characteristics are listed in Table 2. Mesh 1 is rather coarse and is only used to study the convergence of the results with mesh refinement. Very thin elements are required around the cylinders to account

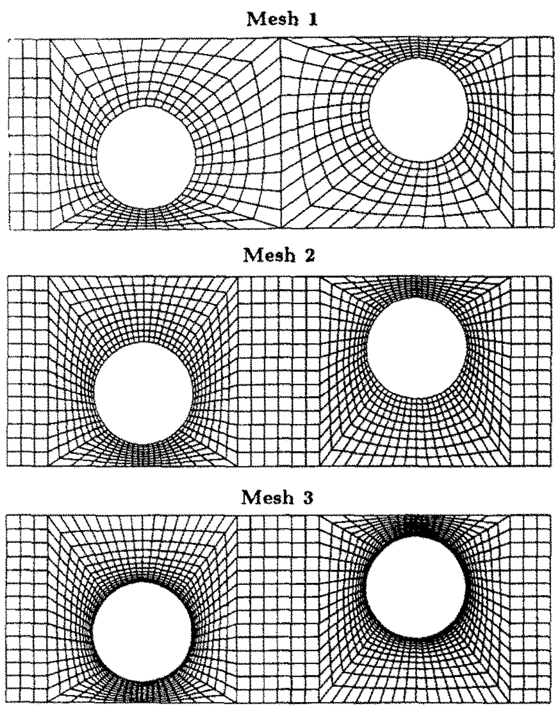

Fig. 20. Finite element meshes.

TABLE 2

Mesh characteristics

Mesh	Number of elements	Number of velocity nodes	Degrees of freedom
1	648	2751	38291
2	1248	5227	73137
3	1728	7147	100487
			(16140) [a]

[a] For the generalized Newtonian problems.

for the stress boundary layers likely to develop in the vicinity of the cylindrical walls. Mesh 3 was used for all the generalized-Newtonian calculations.

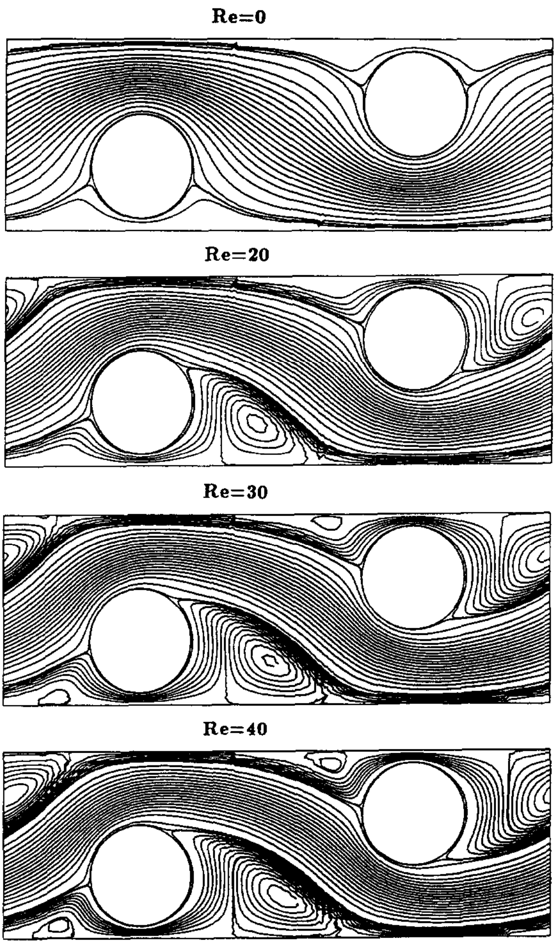

Fig. 21. Numerical simulation of Newtonian flow for $D = 1.5$ mm.

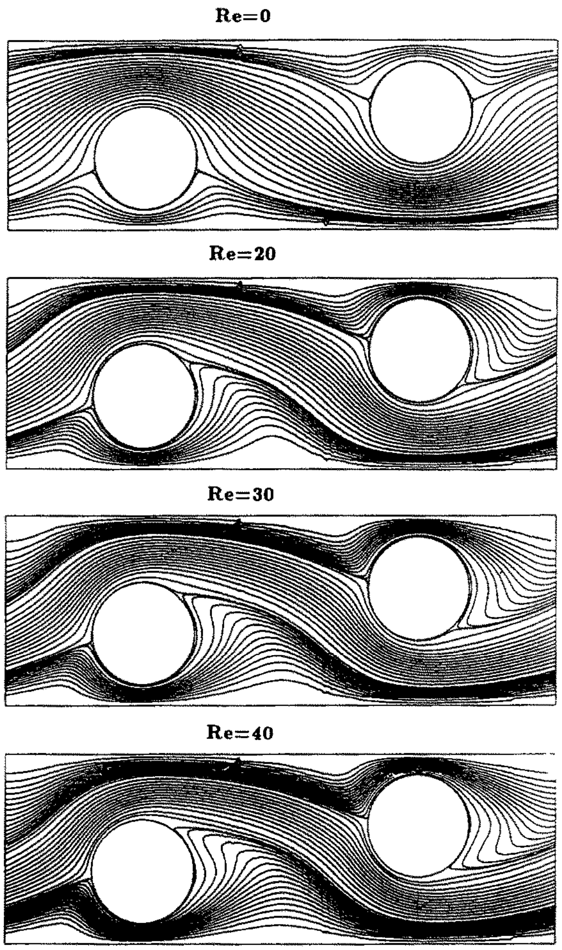

Fig. 22. Numerical simulation of Newtonian flow for $D = 2.5$ mm (geometry $W1$).

To study the sensitivity of the flow to the size of the gap between the cylinders and the wall D, we use different gap thicknesses varying from 1.5 up to 5.25 mm which corresponds to the symmetric case. The computed streamlines for a Newtonian liquid and $D = 1.5$, 2.5 (geometry $W1$), 3.5 (geometry $W2$) and 5.25 mm are given in Figs. 21–24. Flow is from left to right in all pictures. Notice that the wiggles observed in some of the plots are generated by the contours program and are not real. For low values of Re, it is found that the streamlines are essentially the same as those at zero Re with no perceptible change in the position of the divided streamline, in agreement with the flow-visualization results. At higher Re, the divided streamline moves farther from the channel walls, especially downstream where we observe different recirculation patterns depending on the geome-

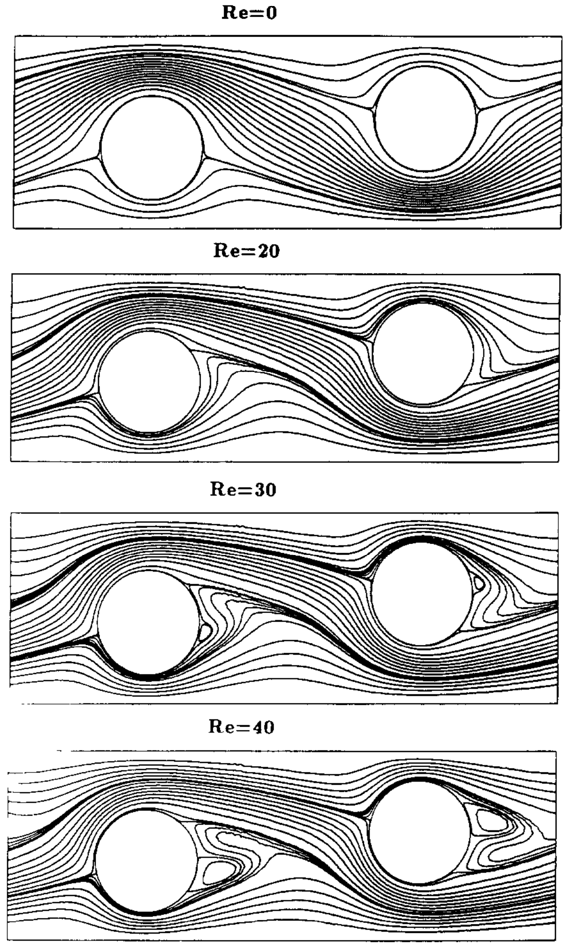

Fig. 23. Numerical simulation of Newtonian flow for $D = 3.5$ mm (geometry $W2$).

try. The simulations in Figs. 22 and 23 are in satisfactory agreement with the flow-visualization results, indicating that three-dimensionality effects are not very important at the central plane where the flow-visualization pictures are taken. It is interesting to note that, when D is small, a vortex similar to that obtained experimentally with $W1$ near the vertical wall (Fig. 7(ii)) appears upstream (see Fig. 21).

The predicted dimensionless pressure drops ΔP^* are plotted against Re in Fig. 25. Notice that ΔP^* is proportional to $\Delta P/Q$. ΔP^* is constant at low Re in agreement with the experimental measurements of Fig. 9, and increases at higher values of it. As with the experiments, when Re is low, the pressure drop decreases as we reduce D. This is not true, however, at higher Re.

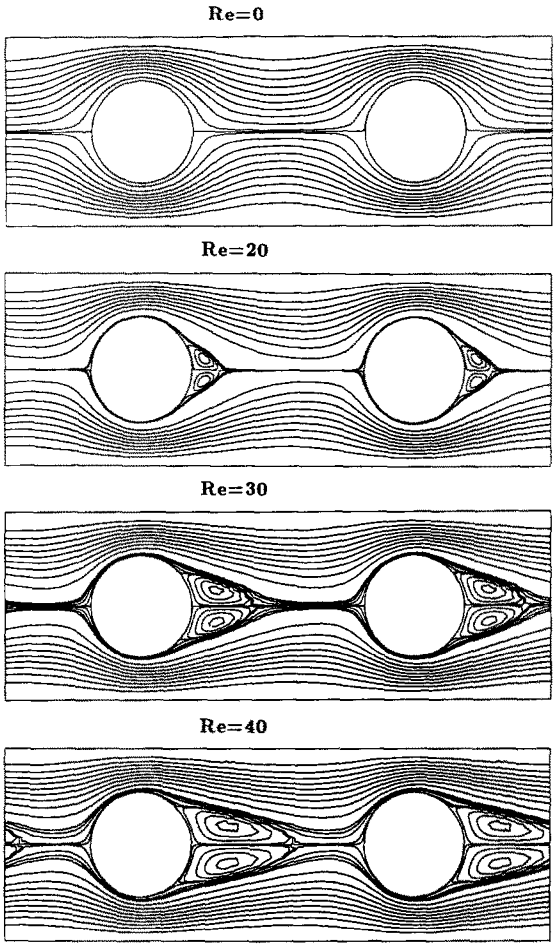

Fig. 24. Numerical simulation of Newtonian flow for $D = 5.25$ mm (symmetric case).

Another interesting quantity is the amount of fluid Q_s passing through the narrow gap between the cylinders and the walls relative to the total flow rate. The results for various values of D are plotted vs. the Re in Fig. 26. Q_s/Q is initially constant and then increases with the Re. As expected, the flow through the gap decreases rapidly as D is reduced.

The computed streamlines for the 1500 ppm X fluid are shown in Fig. 27, for different values of Re. They are in good qualitative agreement with the experimental results of Jones and Walters [5]. The flow patterns are similar to those obtained for the Newtonian case with $W1$ and $W2$. Shear thinning leads to the appearance of the downstream vortices at relatively low Re. Figure 28 compares the calculated values of $\Delta P/Q$ for different gap thicknesses with the experimental data given in Ref. 5. $\Delta P/Q$ increases

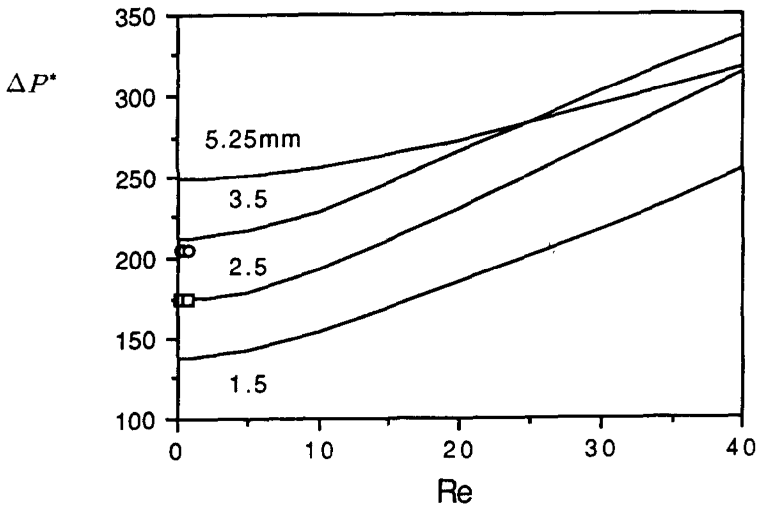

Fig. 25. Calculated dimensionless pressure drops for a Newtonian liquid and various gap thicknesses: □, experimental data for $D = 2.5$ mm; ○, experimental data for $D = 3.5$ mm.

slightly with D. The simulation curves agree rather well with the experimental points indicating that the three-dimensionality effect is not too severe. (Notice that end effects are ignored in our simulations.) The calculated Q_s/Q are compared with the experimental data of Jones and Walters [5] in Fig. 29. They determine Q_s from the flow-visualization pictures by following the divided streamline down to a region where a Poiseuille-flow profile can

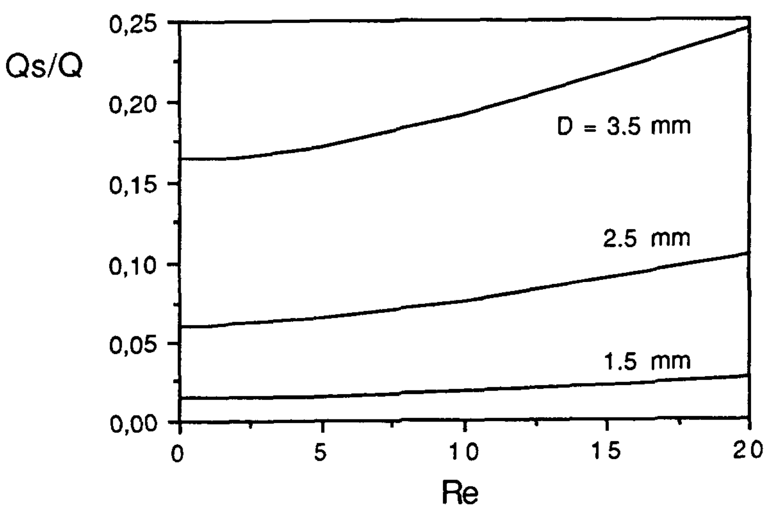

Fig. 26. Calculated values of Q_s/Q for the Newtonian liquid and various gap thicknesses.

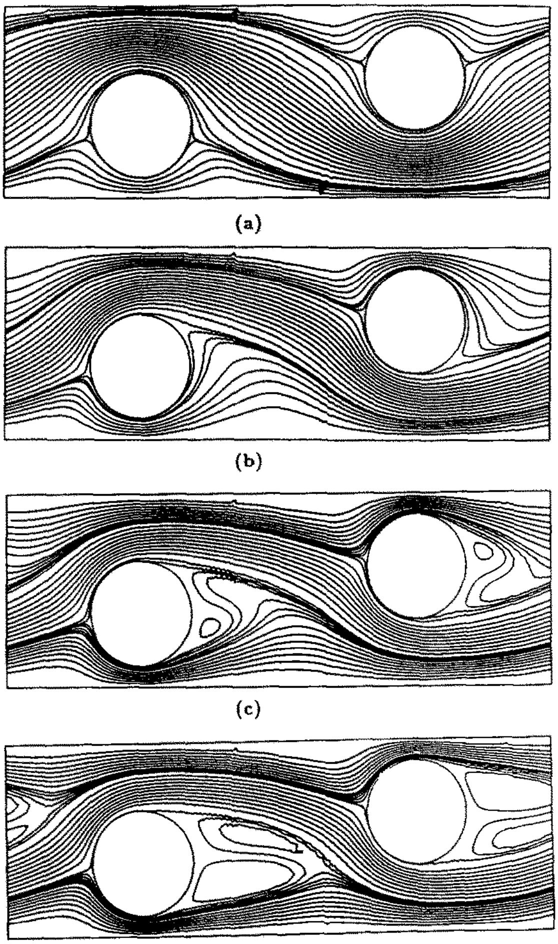

(a)

(b)

(c)

(d)

Fig. 27. Numerical simulation of the flow of the 1500 ppm X fluid in $W1$ with the Bird–Carreau model: (a) $Re = 0.001$ ($Q = 0.5$ cm^3 s^{-1}); (b) $Re = 27.2$ ($Q = 50$ cm^3 s^{-1}); (c) $Re = 46.7$ ($Q = 75$ cm^3 s^{-1}); (d) $Re = 72.4$ ($Q = 103$ cm^3 s^{-1}).

be assumed. As in the Newtonian case, Q_s/Q increases as the volumetric flow rate increases. Among the different gap thicknesses examined, $D = 2.0$ mm gives the best agreement with the experiments indicating that the effective gap thickness may be smaller than 2.5 mm although it must be conceded that the procedure of determining Q_s from photographs is not very precise.

Figure 30 contains perhaps the most important simulations of the present work obtained with the constant viscosity Oldroyd-B model for creeping flow, i.e. for the purely viscoelastic case. Here, we observe that the dimen-

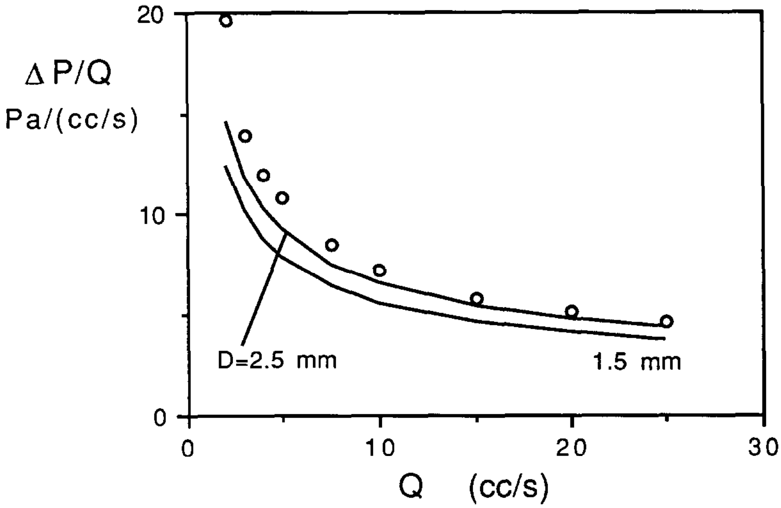

Fig. 28. ($\Delta P/Q$, Q) results with the Bird–Carreau model for the 1500 ppm X fluid in *W*1; ○, experimental data of Jones and Walters [5].

sionless pressure drop initially decreases with the Weissenberg number, *We*, but then increases, in qualitative agreement with the experimental results for the Boger fluids discussed in Section 2 and in line with the drag observations of Walters and Barnes [10]. Note that this general finding is independent of the size of the mesh. Meshes 2 and 3 give practically the same results and the

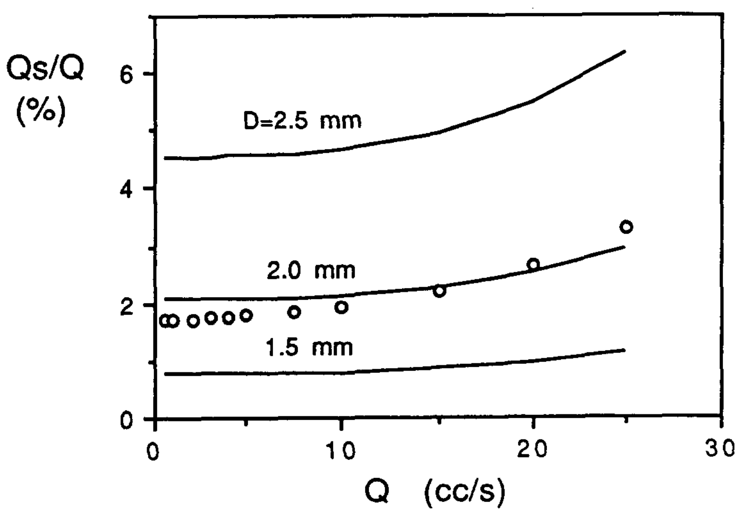

Fig. 29. Calculated values of Q_s/Q with the Bird–Carreau model for the 1500 ppm X fluid in *W*1; ○, experimental data of Jones and Walters [5].

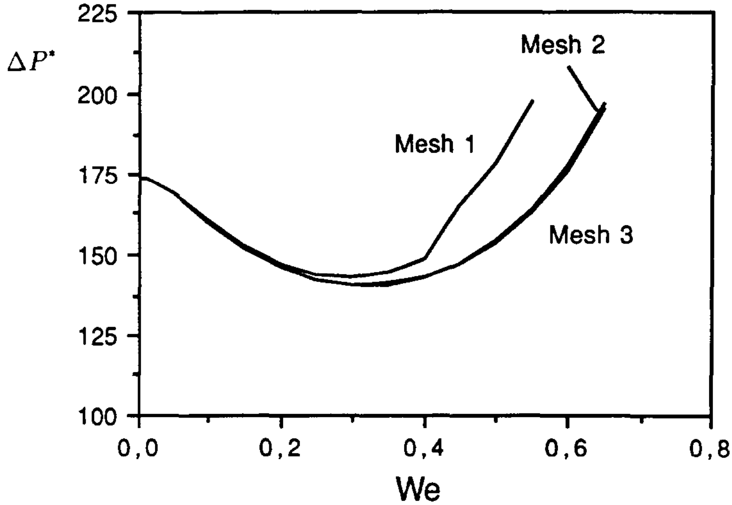

Fig. 30. Calculated values of ΔP^* with the Oldroyd-B model at zero *Re* (geometry *W*1).

solution is assumed to have converged, at least for the relatively low *We* considered here. At higher *We* the stress boundary layers around the cylinders grow stronger and the radius of convergence of the method becomes very small and it is impractical to continue. Further refinement is necessary if results at higher *We* are desired. In addition to mesh refinement, another test for the numerical findings is to decrease the streamline upwinding coefficient in order to ensure that the minimum is not a consequence of the artificial stress diffusivity. Indeed, when we reduce the streamline upwinding coefficient, ΔP^* decreases slightly but the minimum is preserved in all cases.

The computed streamlines for zero *Re* are shown in Fig. 31 for different *We*. At low *We*, the flow field is, of course, similar to that of the creeping Newtonian case and is not significantly affected as we increase *We*, in accordance with the experimental observations with the Boger fluids in Figs. 15 and 16. (A more careful examination reveals that the upstream divided streamline initially moves farther from the wall and then starts shifting to the opposite direction, whereas the downstream divided streamline remains essentially unaffected.) The numerical results beyond the critical flow region where the minimum occurs have been most interesting. Figure 31 shows that the flow characteristics are similar to those obtained experimentally with the P fluids in Figs. 17 and 18. The fluid appears to be reluctant to pass through the narrow channels and this is attributed to extensional-viscosity effects which become very important at high *We*. Similar results are obtained if we keep the elasticity number constant and increase the Reynolds number

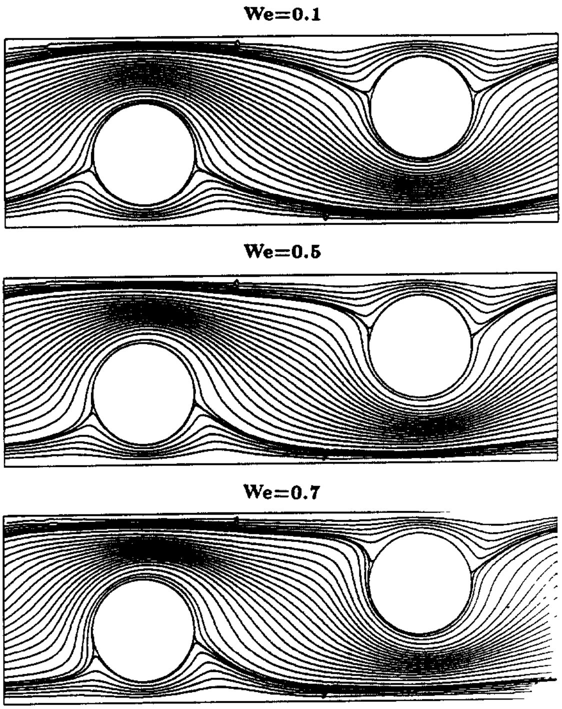

Fig. 31. Streamlines obtained with the Oldroyd-B model at zero Re (geometry $W1$).

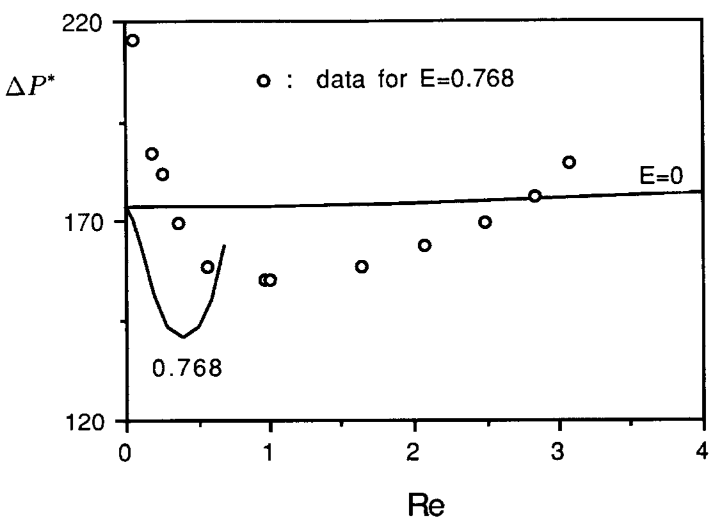

Fig. 32. Calculated ΔP^* with the Oldroyd-B model in geometry $W1$; ○, experimental data with B112.

instead. The elasticity number, defined by

$$E = \frac{We}{Re} = \frac{4\eta\lambda}{\rho A^2}, \tag{19}$$

provides a ratio of elastic vs. inertial effects and is independent of the flow rate. The value of E for B112 in $W1$ is 0.768. Figure 32 shows that a minimum of ΔP^* is again encountered as we increase Re, in qualitative agreement with the experimental data of Fig. 13. Notice that, when plotting ΔP^* against Re, the discrepancies between simulations and experiments are exaggerated at low Re. In contrast to the creeping flow solution and the experiments, the reluctance of the fluid to pass through the narrow channels is manifested before we reach the critical flow region in which ΔP^* becomes minimum. Again, if results at higher Re are desirable, mesh refinement is in order.

3.4. Conclusion

A finite-element technique has been used to simulate Newtonian and non-Newtonian flow in the model geometries. The agreement between experiment and theory is quite satisfactory in all cases. The calculations with the Oldroyd-B model are able to simulate qualitatively the observed effects of viscoelasticity on the flow characteristics.

4. General conclusions

From a comprehensive computational and experimental investigation of the flow in a channel obstructed by an antisymmetric array of cylinders, we may make the following general observations:

(i) The qualitative agreement between experiment and theory may be considered to be satisfactory, within the acknowledged limitations of present-day viscoelastic simulations.

(ii) For the examined flow conditions and when the Reynolds number is low, the flow rate is higher the closer the cylindrical obstacles are to the walls of the channel (i.e. the smaller the gap D).

(iii) The resistance to flow for constant-viscosity Boger fluids initially decreases with flow rate and then increases as the flow rate is further increased. This increase may be associated with the extensional-viscosity characteristics of the Boger fluids. The extensional-viscosity effect is stronger in geometry $W2$ (i.e. for the higher value of D).

(iv) So far as flow visualization is concerned, there is evidence of a three-dimensional effect for both Newtonian and elastic liquids. However, it is still meaningful to compare the experimental flow characteristics in the central plane with the numerical simulations based on a strictly two-dimensional flow.

(v) Downstream vortices are in evidence at high Reynolds numbers in all cases and an *upstream* vortex can appear under some conditions.

(vi) The acknowledged reluctance of highly elastic liquids to pass through narrow converging channels is clearly in evidence in some of the experiments and the calculations as well.

References

1 T. Cochrane, K. Walters and M.F. Webster, Phil. Trans. R. Soc. London, Ser. A, 301 (1981) 163–181.
2 K. Walters and M.F. Webster, Phil. Trans. R. Soc. London, Ser. A, 308 (1982) 199–218.
3 D.M. Binding, K. Walters, J. Dheur and M.J. Crochet, Phil. Trans. R. Soc. London, Ser. A, 323 (1987) 449–469.
4 S.A. Dhahir and K. Walters, J. Rheol., 33 (1989) 781–804.
5 D.M. Jones and K. Walters, Rheol. Acta, 28 (1989) 482–498.
6 H.A. Barnes, J.F. Hutton and K. Walters, An Introduction to Rheology, Elsevier, Amsterdam, 1989.
7 K. Walters, A.Q. Bhatti and N. Mori, in: D. De Kee and P.N. Kaloni (Eds.), Recent Developments in Structured Continua, Vol II, Pitman, 1990, pp. 182–198.
8 D.V. Boger, J. Non-Newtonian Fluid Mech., 3 (1977/78) 87–91.
9 D.V. Boger and R.J. Binnington, J. Non-Newtonian Fluid Mech., 35 (1990) 339–360.
10 K. Walters and H.A. Barnes, Proc. 8th Int. Congress on Rheology, Naples, Plenum Press, 1 (1980) 45–62.
11 M.J. Crochet, A.R. Davies and K. Walters, Numerical Simulation of non-Newtonian Flow, Elsevier, 1984.
12 J.G. Oldroyd, Proc. R. Soc. London, Ser. A, 200 (1950) 523–541.
13 J.M. Marchal and M.J. Crochet, J. Non-Newtonian Fluid Mech., 26 (1987) 77–114.
14 M.J. Crochet, V. Delvaux and J.M. Marchal, Proc. 3rd Int Conf. Numerical Methods in Industrial Forming Processes, E.G. Thompson, R.D. Wood, O.C. Zienkiewicz and A. Samuelson (Eds.), Fort Collins, Colorado, 1989, pp. 17–22.
15 I. Babuska, Number Math., 20 (1973) 179–192.
16 F. Brezzi, On the existence, uniqueness and approximation of saddle-point problems arising from Lagrange multiplier, RAIRO Num. Anal., 8-R2 (1974) 129–151.
17 A.N. Brooks and T.J.R. Hughes, Comp. Meth. Appl. Mech. Eng., 32 (1982) 199–259.
18 M.J. Crochet, V. Delvaux and J.M. Marchal, J. Non-Newtonian Fluid Mech., 34 (1990) 261–268.
19 V. Delvaux, Ph.D. Thesis, Faculté des Sciences Appliquées, Universite Catholique de Louvain, 1989.